

Probing quantum wells induced above a subsurface nanocavity in copper

O. Kurnosikov, O. A. O. Adam, H. J. M. Swagten, W. J. M. de Jonge, and B. Koopmans

*Department of Applied Physics, Center for NanoMaterials and COBRA Research Institute, Eindhoven University of Technology,
P.O. Box 513, 5600 MB Eindhoven, The Netherlands*

(Received 16 July 2007; revised manuscript received 21 February 2008; published 26 March 2008)

Argon-filled nanocavities embedded in a single crystal of copper near the surface reflect electrons and induce a quantum well (QW) between the nanocavity and the atomically flat Cu(001) surface. The spatial variation of conductance at the surface above the nanocavity was studied by scanning tunnelling microscopy and/or spectroscopy. Interference features were observed over several nanometers at some locations on the surface. In the [100] and [010] directions, the interference fringes propagate over longer distances up to tens of nanometers. In addition to these spatially resolved features, the conductance reveals an oscillatory behavior as a function of energy of injected electrons. A model taking into account the specific shape of the nanocavity, as well as the band structure of copper, allows us to simulate the spatial variation of the conductance in close agreement with the experiment. The modeling demonstrates that not only the specific shape of the subsurface nanocavity reflecting electrons is crucial to explain the observed pattern, but also the anisotropy of the band structure and the phenomenon of focusing of hot electrons connected to it. Our approach opens up opportunities to examine buried nano-objects with scanning tunneling microscopy, and also to study how the anisotropy of a crystal influences the spatial variation of QW properties.

DOI: [10.1103/PhysRevB.77.125429](https://doi.org/10.1103/PhysRevB.77.125429)

PACS number(s): 72.10.Fk, 68.37.Ef, 73.21.Fg, 61.72.J-

INTRODUCTION

Systems with electron confinement have generated considerable interest regarding both fundamental problems and practical applications. Usually, the confinement *inside* a nanostructure in one, two, or three dimensions is considered by which quantum states are induced.¹ However, in a system containing nanoparticles, an additional confinement in one dimension (1D) can occur in between neighboring particles, or in between a nano-object and a nearby macro-object. In this case, one can expect the presence of spatially localized quantum well (QW) states *outside* the nanoparticles. The difference of this case from a common QW system² formed by ultrathin layers is a localization of the QW states in the nanovolume with the confinement in only one dimension. The simplest model of this quasiopen system can be represented by a metal with nonconductive nanoinclusions in the bulk. If the nonconductive nanoinclusions are buried very close to the metallic surface, which can be considered as a border with a very large macro-object, the QW is formed in between the surface and the nanoinclusion. In this paper, we will focus on this kind of system. The near-surface QW states locally affect the electron transport at the surface just above the nanoinclusion and it can be analyzed with the scanning tunneling microscopy and/or spectroscopy (STM/STS) technique. It opens avenues to use this surface-sensitive technique in studying various buried nano-objects and electronic processes appearing under a surface.

It has been already demonstrated that the STM is capable to resolve details under a surface and at interfaces of particular systems, such as steps at a Si interface buried by a thin Pb film due to the formation of thickness dependent 1D QW states,^{3,4} or a single near-surface impurity atom in a semiconductor due to a long electron screening length.⁵ In pure metallic systems, the near-surface single atomic impurities also can be detected with STM exploiting the electrons scat-

tered back to the surface within a distance of the order of the electron mean free path.^{6,7} In this case, the electrons scattered back from the point defects cause interference rings at the surface. Analyzing the diameter of the rings, the location of the impurity atoms in the bulk can be determined. Additionally, this analysis provides the opportunity to judge how the electronic waves propagate in the crystal having a specific band structure. However, it would be much more attractive if the same STM-based approach can be used to characterize near-surface objects, for example, buried nanoparticles.

The present work was inspired by pioneering experiments of Schmid *et al.*⁸ on the electron interference in Al containing nanometer-sized subsurface cavities filled with argon. A spatial variation of the apparent height on the atomically flat surface of Al(111) was observed in the STM images taken above the nanocavities, which is, according to the authors, due to the QW induced under the surface. The spatial size and shape of this variation roughly correspond to the subsurface object reflecting the electrons. Treating the data with a simple particle-in-a-box model, the authors deduce the energy steps between the QW states, the depth of the cavity location, and its size. However, using Cu(111) and Cu(001) surfaces in similar experiments, only ring-shaped interference patterns and no indication of QW states were obtained⁹ because, as speculated, the subsurface reflectors are very small, probably just point defects.

In this paper, we report the results on QW formation at the surface of Cu(001) due to the presence of Ar nanocavities in the bulk close to the surface. We have specifically chosen the copper system in order to see the contribution of anisotropy of the electronic properties to the spatial variation of the QW states. In contrast to the previously reported Al system, Cu reveals a very pronounced angular variation of conductance above the nanocavity. Additionally, high resolution STM images show an interference pattern laterally extending over tens of nanometers away from the location of the nanocavity.

In line with the symmetry of Cu(001), we have observed a fourfold symmetry in the spatial distribution of differential conductance in the vicinity of the nanocavity, which has never been observed before in this kind of experiment. We have found that the specific shape of the subsurface nanocavity reflecting the electrons cannot explain all the details of the observed pattern. The band structure of copper¹⁰ and the phenomenon of focusing of hot electrons^{11,12} connected to it play an important role in the observed spatial variation of the conductance maps. We developed a model taking into account injection, propagation, reflection and interference of electrons, as well as the anisotropy of electronic properties in Cu. From this model, we determined the size and shape of the (001) facet of the nanocavity facing the surface, as well as the depth underneath the surface, in relation to the observed spatial variation of surface conductance.

EXPERIMENT

The experiment was carried out in a multichamber ultra-high vacuum system with a base pressure below 5×10^{-11} mbar, which includes a low-temperature STM. The Cu(001) single crystal surface was cleaned with a common sputtering-annealing procedure until a sharp $p(1 \times 1)$ low-energy electron diffraction pattern is achieved, and then it was intensively bombarded by Ar^+ ions at 2 keV with a current density of $0.3\text{--}0.5 \text{ A/m}^2$ for 15 min, followed by annealing at 900 K for 5 min. We also varied the time of bombardment, as well as the duration of annealing to ensure that the presence of the observed effect directly relates to the amount of argon. The intense bombardment implants argon in the near surface region, while the annealing induces the diffusion of argon atoms and their subsequent aggregation. The temperature quenching after the short annealing time freezes the situation when part of argon is still captured under the surface in the Ar-filled nanocavities. Longer annealing leads to the diffusion of all argon to the surface. Annealing also restores the near-surface crystalline ordering of Cu destroyed during the bombardment. Our successful formation of subsurface cavities in the Cu crystal, in contrast to the results of Schmid *et al.*,⁹ can be understood by the fact that we used a very intense Ar beam during bombardment, which probably is a key to achieve this result. The sample prepared in this way was finally transferred from the preparation chamber to the STM connected to the same UHV system and operating at 77 K. Electrochemically etched W tips were cleaned in UHV by e-beam bombardment. Differential conductivity dI/dV spectra were recorded under an open feedback loop using a lock-in amplifier with a modulation of 50 mV added to the bias voltage. Moreover, area maps of the dI/dV signal were recorded simultaneously with constant-current imaging during surface scans.

RESULTS

Constant-current STM images of the samples reveal an atomically flat Cu(001) surface with spots of several nanometers large (not shown here) randomly distributed over the surface. However, the apparent height of these spots is sig-

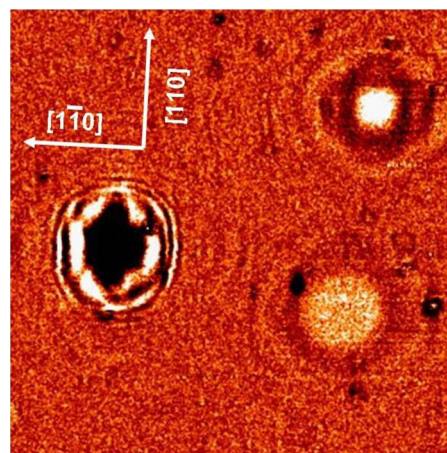


FIG. 1. (Color online) Spectroscopy dI/dV map of Cu(001) after Ar bombardment and annealing. The area is $35 \times 35 \text{ nm}^2$ and the conductivity is measured at 220 mV and 2.0 nA. The spots reveal various contrasts predominantly in the center of the different spots (see the text for more details).

nificantly lower than the typical atomic size, which means that no atoms or molecules lying on the surface can be associated with the observation. The differential conductance or dI/dV map reveals much more features of these nanospots. Figure 1 presents a typical example of three spots observed at different locations and at the same bias voltage. Remarkably, the magnitude of the dI/dV signal in the center of the spot is largely different when comparing these spots. The spot in the right bottom corner shows a homogeneous distribution of the conductance within a circle of about 8 nm in diameter. The spot in the upper right corner reveals a stronger variation of the signal and a slight nonhomogeneous angular distribution of differential conductance. The surrounding contour slightly differs from circular symmetry. The third spot on the left side has the strongest variation of the conductance and the areas of suppressed conductance are elongated along the [110] direction. Additionally, all spots are surrounded with interferencelike fringes. Inspecting other locations, we have found spots even with an almost rectangular or square shape. Note that the impurity atoms accidentally present at the surface of the same sample are imaged as simple point defects without extra features around them. These impurities also do not affect the interference fringes around the spots (see again Fig. 1).

An STM scan at low bias voltage with higher resolution elucidates extra details. Figure 2 presents the image formed by the uncompensated current. This specific regime is more sensitive to fast variations of current caused by the short-range spatial variation of conductance, while gradual changes are effectively compensated by a feedback. Thus, the structure close to the center of the spot is suppressed; however, the beams of fringes running far away from the observed surface structure in the [100] and [010] directions are well visible. The fringes can be very long ranged, and may be visible over a distance up to 10 nm. Additionally, the image confirms that there are no extra local inclusions in the center of the spot. Therefore, the nature of the complicated spot structures should originate from an electronic effect rather than a simple relief modulation.

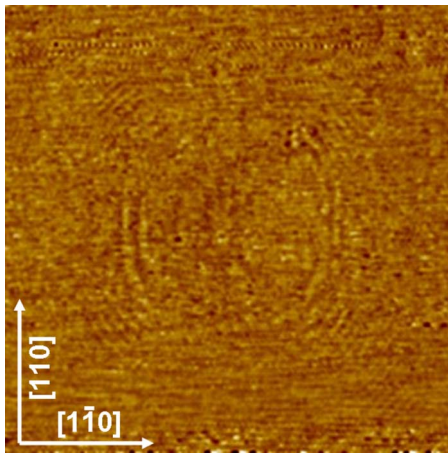


FIG. 2. (Color online) STM image of the Cu surface built with the current signal. The quasisquare surrounding fringes are about 5 nm far away from the center. Radial beams of fringes run outside the quasisquare surrounding over a distance of 10 nm in the $\langle 100 \rangle$ directions. The field of view is $20 \times 20 \text{ nm}^2$, bias voltage 9.0 mV, and current 3.0 nA.

These observations lead to the hypothesis that the observed interference features do not relate to oscillations of charge density^{13,14} of surface states in the vicinity of a scattering center, but they are likely the result of electron interference due to the presence of a subsurface nanoinclusion reflecting bulk electrons. It is expected that the magnitude of the dI/dV signal as well as its specific spatial distribution reflects somehow the size, shape, and depth of location of the nanoinclusion. Later in this paper, we will come back to this point in the analysis of these details.

If the observed features are really the result of electron interference, which strongly depends on the wavelength of electrons, we should expect a periodic change in the observed pattern at different energies of injected electrons. We have obtained a direct proof of this behavior by monitoring the differential conductance dI/dV at variable bias voltages. The sequence of dI/dV maps above a typical subsurface nanoinclusion at different voltages is presented in Fig. 3. Although these data do not show the features with high resolution, such as the long radial beams visible in Fig. 2, the inner part of the surface pattern reveals a strong and periodic variation with the applied bias voltage. Also, the characteristic fourfold symmetry, corresponding to the Cu crystalline lattice orientation, is clearly visible in the inner part. The sequence of the images shows a variation of the pattern with a period of about 0.3 V in this particular case.

The periodic variation is also registered in a conductance curve measured in the center of the object. Figure 4 presents the typical dI/dV curve for both the clean copper surface and at the center of the feature. Since for this measurement another spot was selected as used in Fig. 3, it shows a different periodicity, which in this case is about 0.5 V. This observation manifests that not only the specific spatial variation of the dI/dV map characterizes each spot individually, but also the periodicity of the dI/dV signal versus the electron energy is a parameter that directly relates to the depth of the subsurface reflector of electrons. In the following section, we will

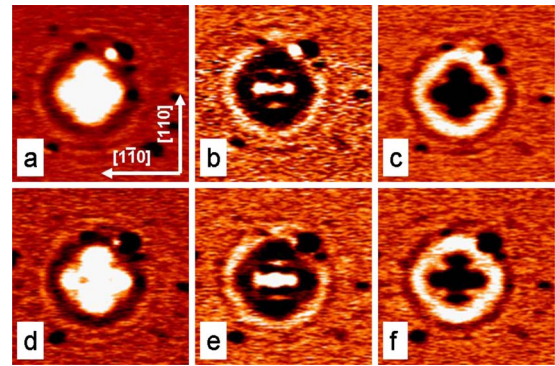


FIG. 3. (Color online) Conductance maps above a nanocavity measured at different bias voltages: (a) +0.3, (b) +0.4, (c) +0.5, (d) +0.6, (e) +0.7, and (f) +0.8 V. The tunnel current is 1.2 nA. The scan area is $16.6 \times 16.6 \text{ nm}^2$. The periodicity of the images is about 0.3 V.

further analyze our data using a model that captures the basic mechanism behind these interference effects.

MODEL

Based on the experimental results, we developed a model describing the basic processes of electron interference. It will provide a simulation of spatial distributions of surface conductivity that can be directly compared with our STM data. Our aim is to basically understand which physical phenomena are responsible for the complicated spatial distribution of the surface conductivity seen in the experiment. At the same time, we realize that for a detailed description of the system a more complicated approach could be used. Before presenting the model in more detail, we will first consider the basic physical processes taking place in our system.

The surface of the nanocavity separating the conductive (copper) and nonconductive (argon) mediums serves as an effective reflector of hot electrons injected by an STM tip at the surface. The hot electrons, injected in the copper single crystal at its surface, propagate in the bulk without scattering up to a distance of tens of nanometers.¹⁵ A schematic draw-

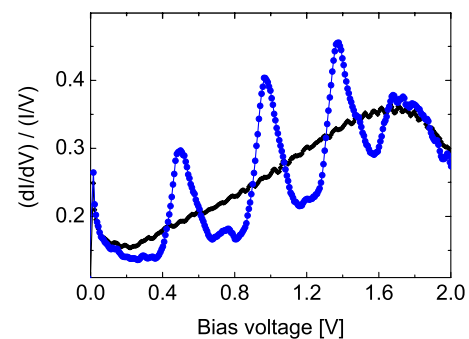


FIG. 4. (Color online) Normalized dI/dV measured in the center of the spot reveals strong oscillations (blue or dark-gray circles). A similar measurement at the clean Cu surface far away from the nanocavity shows no oscillations (black diamonds).

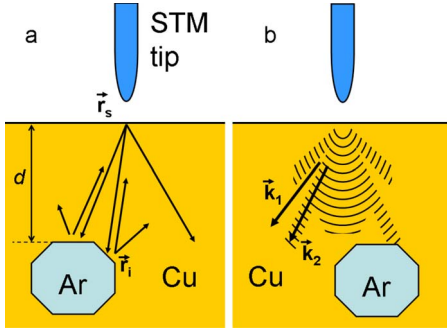


FIG. 5. (Color online) Schematic diagram of the processes considered in the model: (a) injection, propagation, and reflection of the electrons in copper; and (b) propagation of the electronic wave in the anisotropic medium. The electrons injected at the surface in a cone form a nonspherical wave front with the decay factor dependent on the direction of propagation. In some directions, corresponding to \mathbf{k}_1 , the propagation is forbidden and the wave decays fast, whereas in other directions, for example, corresponding to \mathbf{k}_2 , the wave concentrates due to the focusing effect.

ing of the propagation and reflection of electrons is presented in Fig. 5(a). We assume that electrons are injected in a point of the surface just under the tip position \mathbf{r}_s , and we neglect all the effects originated from the tip shape or its electronic properties. Each point of the nanocavity interface \mathbf{r}_i reflects the hot electrons in different directions. The electrons reflected back to the injection point interfere with the incoming electron wave at the surface, and the resulting transmission of the system for the electron transport varies according to the interference rules. The multiple reflections between the surface and interface provide an ideal condition of QW formation. However, in a quasiopen system, the efficiency of the multiple reflections is low, and we will consider only a single reflection from the interface.

The electrons injected and propagating in copper form a nonuniform electron wave. The main cause of the complicated angular and intensity distribution of the electron wave is related to the anisotropy of the bulk crystal, although the tunneling effect also contributes in this nonuniformity due to a selection of k vector¹⁶ by the tunnel probability at the injection point. The anisotropy not only leads to the dependence of electron wavelength on the direction of propagation, but also to a variation of the decay of the wave amplitude in this propagation direction. For example, in copper, there are no available electronic states for k vectors in the $\langle 111 \rangle$ directions at energies close to the Fermi level. As a result, the electron wave strongly decays and does not propagate in these directions. Alternatively, in some cases, the differences in the vectors of phase and group velocities lead to so-called focusing effects when the electron wave concentrates along some specific directions when propagating over large distances.^{11,12,17} Additionally, we have taken into account that the tunneling effect already provides a nonuniform initial distribution of the electron waves at the injection point. Schematically, the propagation of the electronic wave is presented in Fig. 5(b). In this figure, the wave vectors \mathbf{k}_1 and \mathbf{k}_2 correspond to the directions with high and low decay factors, respectively. The difference in the decay forms a

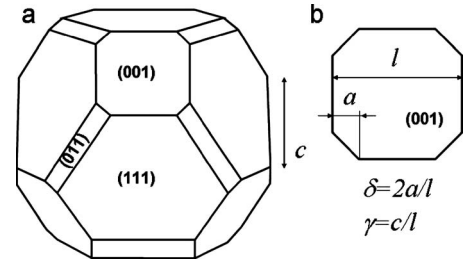


FIG. 6. Specific shape of the nanocavity in single-crystalline copper as used in the calculations: (a) Wulff construction, and (b) (001) facet of the nanocavity which is closest to the surface. The shape of the facet and nanocavity is determined by the parameters l , δ , and γ (see the text).

very developed profile of the resulting angular distribution of amplitudes of the propagating wave, and profoundly affects the resulting interference when the electron waves are reflected back to the injection point.

Let us now consider the shape of the reflecting nanocavity surface. In our experiments, the nanocavities are formed by subsurface segregation of argon atoms implanted into single-crystalline copper caused by annealing. The anisotropy of the interface free energy should lead to a complicated specific shape of the nanocavity similar to a Wulff construction,¹⁸ which can be well determined for a large object. However, in the case of a nanocavity, it could very well be that the actual shape can vary with the volume. An additional statistical deviation from high-symmetrical shapes, which is probably related to elongated spots sometime observed in the experiment (see, for example, the left spot in Fig. 1), makes the description of the nanocavity extremely complicated. Nevertheless, for the sake of simplicity, we will consider only a symmetric shape of the nanocavity with three kinds of facets corresponding to (001), (111), and (110), including all other equivalent planes [Fig. 6(a)]. This simple approach needs only three parameters to completely determine the buried nano-object. Two of them completely determine the size and shape of the upper (001) facet: the lateral size of the facet along the $[110]$ direction l and the ratio $\delta = 2a/l$, where $2a$ is the reduction in length of the rib due to the truncated corner by the (110) facet [see Fig. 6(b)]. The third parameter $\gamma = c/l$, where c is the length of the (110) facet, determines not only its shape, but also the asymmetry of the (111) facet. The depth of the nanocavity d , which is taken from the top of the cavity up to the upper surface of the bulk metal, plays a crucial role in forming the interference pattern at the surface. In our analysis of the data later, we will determine d by using the period of oscillation of the differential conductivity with the energy of the injected electrons as follows:

$$d = \frac{\pi}{\Delta E} \frac{\partial E}{\partial \mathbf{k}}, \quad (1)$$

where ΔE is the experimentally determined oscillation period, and $\partial E / \partial \mathbf{k}$ is derived from the band structure of copper $E(\mathbf{k})$ along the $[001]$ direction.

We describe the electron injection, propagation, and reflection together via the corresponding functions $G(\mathbf{r}_s - \mathbf{r}_i)$,

$P(\mathbf{r}_s - \mathbf{r}_i, E)$, and $R_n(\mathbf{r}_s - \mathbf{r}_i)$, respectively, where \mathbf{r}_s is the coordinate of the injection point at the surface, \mathbf{r}_i is the coordinate of the considered point at the interface with the nanocavity, E is energy of injected electrons, and n is the index selecting the considered facet. Function $G(\mathbf{r}_s - \mathbf{r}_i)$ describes the angular distribution of electrons at the injection point.^{16,17} Function $R_n(\mathbf{r}_s - \mathbf{r}_i)$ describes the angular scattering at each facet n . These functions contain effective parameters to model different widths of distributions.

The most crucial function is the propagation function $P(\mathbf{r}_s - \mathbf{r}_i, E)$. Within our simplified approach, we build it as a product of the amplitude $A(\mathbf{r}_s - \mathbf{r}_i)$ and phase factor $\exp[2i\mathbf{k} \cdot (\mathbf{r}_s - \mathbf{r}_i)]$ as follows:

$$P(\mathbf{r}_s - \mathbf{r}_i, E) = A(\mathbf{r}_s - \mathbf{r}_i) \exp[2i\mathbf{k} \cdot (\mathbf{r}_s - \mathbf{r}_i)], \quad (2)$$

where \mathbf{k} is wave vector of the electron determined by the band structure of copper $E(\mathbf{k})$. The function $A(\mathbf{r}_s - \mathbf{r}_i)$ describes the amplitude of the electron wave function. For the simplest isotropic case, the function should be proportional to $1/|\mathbf{r}_s - \mathbf{r}_i|$. However, we modified $A(\mathbf{r}_s - \mathbf{r}_i)$ in order to take into account the phenomena originating from the anisotropy of electronic properties. Although it is difficult to express it in a compact form, the main idea is quite simple. A different decay of electron waves is assumed in different crystallographic directions. The decay in various directions can be extremely strong corresponding to the absence of electronic states determined by the band structure, or very weak when focusing the electron waves mainly in the directions corresponding to the flat areas on the isoenergetic surface in the reciprocal space.^{12,17} To determine the amplitude factor, we take into consideration the shape of the isoenergetic surface in k space, which is also determined by the band structure $E(\mathbf{k})$. A higher amplitude is additionally assigned to $A(\mathbf{r}_s - \mathbf{r}_i)$ into directions corresponding to a strong ‘‘focusing effect’’ discussed earlier. This artificial approach is not precise, but it allows us to take into account these complicated phenomena in a relatively elementary way instead of a direct calculation of wave evolution in an anisotropic crystal.

The angular distribution of electrons injected at the surface $G(\mathbf{r}_s - \mathbf{r}_i)$ originates from the k -vector selection at the tunneling process. In reality, it depends in a complicated way on bias voltage, electron structure of sample and tip, as well as the tip shape. However, we define it by the simple function $G = \exp(-\theta^2/2\theta_0^2)$, where θ_0 is the effective injection angle, and θ is the angle formed between the normal to the surface and $\mathbf{r}_s - \mathbf{r}_i$.

The function $R_n(\mathbf{r}_s - \mathbf{r}_i)$ also has been chosen in a phenomenological way to model different possible spatial distributions of scattering at the facets. We used functions $\cos(\theta_n)$ for the $\{001\}$ and $\{110\}$ facets, where θ_n is the angle between $\mathbf{r}_s - \mathbf{r}_i$ and the normal to a particular facet indexed with n . For the $\{111\}$ facets, we used a modified function $\cos(\theta_n)\sin(\theta_n)$ to exclude reflections in the $\langle 111 \rangle$ directions which are not allowed. We realize that the way we represent the function R_n is highly schematic in our model. However, the implementation of R_n is definitely necessary to yield a qualitative match with our data, which, given the arguments above, justifies this approach.

Besides this, we introduce a function $w(E)$ describing the energy window which should be taken into account due to the measurement technique using a lock-in amplifier and the ac excitation added to the dc bias voltage. The resulting transmission $T(\mathbf{r}_s)$ of the system for the electron waves injected in each point of the surface \mathbf{r}_s is proportional to the absolute value of the sum of all the complex amplitudes of incoming and reflected waves from all the directions using the following functions:

$$T(\mathbf{r}_s) \propto \left| 1 + \int \int_{\mathbf{r}_i, E} G(\mathbf{r}_s - \mathbf{r}_i) P(\mathbf{r}_s - \mathbf{r}_i, E) \times R_n(\mathbf{r}_s - \mathbf{r}_i) w(E) d\mathbf{r}_i dE \right|^2. \quad (3)$$

The variation of conductance, which is assumed to be proportional to the dI/dV signal, is determined by this transmission function $T(\mathbf{r}_s)$. In spite of the simplifications we made to build the expression for $T(\mathbf{r}_s)$, we obtained a model which can be straightforwardly used for direct comparison with our data. The next section will not only aim for extracting the facet parameters when using this model, but will also help the reader in evaluating the basic numerical results in relation to the geometry and dimension of the cavities.

DISCUSSION

Because none of the parameters of the nanosystem l , δ , γ , and d are known *a priori*, we should carefully address how each parameter affects the surface differential conductance. First, our calculation shows that the dimension and shape of the $\{001\}$ upper facet described by the parameters l and δ strongly affect the spatial distribution of differential conductance. Secondly, the size and shape of $\{110\}$ and $\{111\}$ facets described by γ do not lead to significant changes that could justify a reliable and precise extraction of γ from comparison with our data. Nevertheless, at low bias voltages, this parameter becomes crucial to form the long-range lateral beams of interference fringes, as we will see later.

Below, we present the spatial distribution of the surface conductance obtained with different parameters l , δ , with γ fixed as explained earlier, and with the same depth d as determined quite precisely using Eq. (1). For the calculations presented below, we will use the experimental data shown in Fig. 3 to illustrate the typical features covered by our calculations, as well as to show how to find quantitative numbers for the system parameters. Note that the parameters we will find below do specifically relate to a particular object. When we would have chosen another spot, other values of parameters would be found accordingly.

For this set of data revealing $\Delta E = 0.3$ eV, the depth d of the nanocavity is found to be 9.1 nm and will be fixed in the following calculations. Figure 7 illustrates how the size of the upper facet l determines the spatial distribution of the differential conductivity. The nanocavity with $l = 0.5$ nm induces a well pronounced ringlike pattern [Fig. 7(a)] with a faint residual pointlike fine structure. A very big size of the upper facet with $l = 10$ nm leads to an almost homogeneous

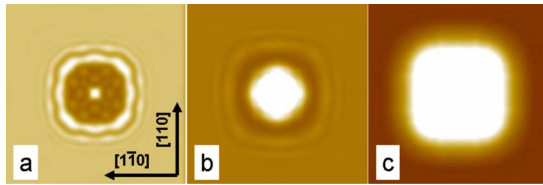


FIG. 7. (Color online) Simulated conductance pattern showing the dependence on the size l of the upper facet of the nanocavities: (a) $l=0.5$ nm, (b) $l=3$ nm, and (c) $l=10$ nm. The extra point modulation in (a) is an artifact of calculation. The field of view is 15×15 nm². For all cases, the upper (001) facet of the nanocavity is placed $d=9$ nm deep below the surface, $\delta=0.4$, $\gamma=1$.

distribution of the differential conductance across a large area [Fig. 7(c)]. The case of $l=3$ nm, which is qualitatively rather close to the experimental observation shown in Fig. 3(a), is presented in Fig. 7(b). A similar calculation has been done when varying the parameter δ describing the upper facet truncation. Figure 8 presents two extreme cases of $\delta=0$ and $\delta=1$. The case of $\delta=0$ corresponds to the situation when the $\{110\}$ facets are completely shrunk [Fig. 8(a)]. The opposite case of $\delta=1$ with the smallest possible $\{111\}$ facets is presented in Fig. 8(b). When we again compare this to Fig. 3(a), it is clear that we are in between these two extreme cases, and may be a little bit closer to case (a). By further calculations at variable bias voltage, upon a variation of l and δ , we were able to find a match with our experimental result when $l \approx 2.8$ nm, $\delta \approx 0.4$, and $d \approx 9.1$ nm. As mentioned before, the parameter γ has been chosen around 1 since it cannot be determined precisely. The series of simulated images for different energies of the injected electrons is presented in Fig. 9. This series is similar to the set of experimental images presented in Fig. 3 in terms of all the specific features, the specific shape, symmetry, as well as the periodicity. However, it is also clear from the images that we cannot get a complete correspondence using our simplified approach.

The essential adequacy of our phenomenological model is further illustrated by the simulation of tiny details, for example, in the long-range interference fringes presented in Fig. 2. Figure 10 presents the simulated image. This image was obtained under the assumption of a high coherence of the electron wave injected at low bias voltages and the en-

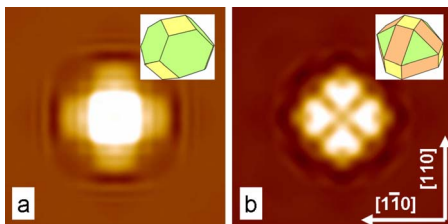


FIG. 8. (Color online) Simulated patterns for two different shapes of the nanocavity: (a) the case of $\delta=0$ with maximal $\{111\}$ facets and completely shrunk $\{110\}$ facets, and (b) $\delta=1$ with maximal $\{110\}$ facets and minimal $\{111\}$ facets. The schematic shape of the nanocavity for each case is shown in the insert. Field of view is 15×15 nm². For both cases, $l=3$ nm and $d=9$ nm.

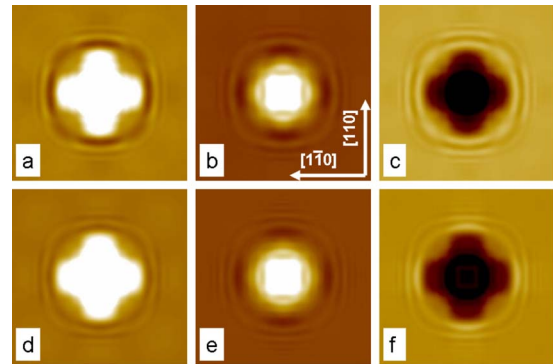


FIG. 9. (Color online) Simulated conductance of the surface above the nanocavity with optimized shape at different energies of injected electrons: (a) $E=+0.3$ eV, (b) $E=+0.4$ eV, (c) $E=+0.5$ eV, (d) $E=+0.6$ eV, (e) $E=+0.7$ eV, and (f) $E=+0.8$ eV. The simulated scan area is 15×15 nm², $l=3$ nm, $\delta=0.4$, and $d=9$ nm.

hanced influence of the focusing effect. Note that the experimental data presented in Fig. 2 were obtained also at relatively low bias voltage. The long radial beams originate from the interference of electrons reflected from $\{110\}$ facets. The $\langle 110 \rangle$ directions correspond to the directions of focusing of electron waves in Cu, by which an interference pattern is formed over a long distance from the nanocavity. However, to obtain this result by simulation, we have to readjust the parameters related to electron propagation and reflection in the model as compared to those used for the simulation of the pattern presented in Fig. 9. It reflects that our phenomenological model is not completely universal due to rather severe assumptions.

Obviously, our model has the potential to be improved. Based on the simplifications discussed above, the model is very efficient in terms of calculation time. It allows us to perform a variation of parameters to find the size, shape, and

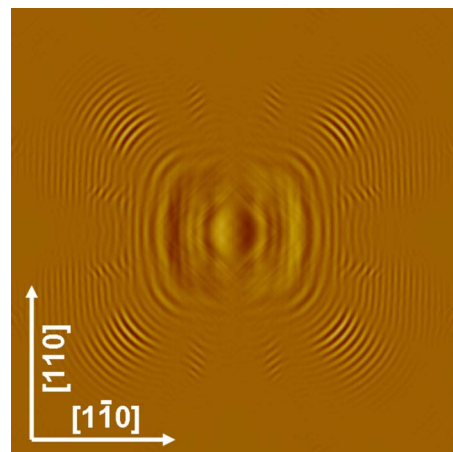


FIG. 10. (Color online) Simulation showing that the interference effects can be detected over a long range in some particular directions. To get the similarity with the experimental results presented in Fig. 2, the image is formed by the derivative of the simulated conductance. $l=2.2$ nm, $\delta=0.4$, $\gamma=0.2$, and $d=5$ nm. The simulated scan area is 20×20 nm².

depth of nanoentities. The main simplification is the implementation of effective functions $G(\mathbf{r}_s - \mathbf{r}_i)$, $P(r_s - r_i, E)$ and $R_n(\mathbf{r}_s - \mathbf{r}_i)$. Within an improved approach, the exact description of the wave propagation should be done by solving a differential wave equation for the anisotropic case. Similarly, describing the injection, instead of the effective function $G(\mathbf{r}_s - \mathbf{r}_i)$ to represent the angular distribution of electrons, a more advanced approach can be done by which possibly a better correspondence of calculated and experimental results is expected. As to the shape of the nanocavities, we assumed a fully symmetric shape that is determined by only three parameters. However, sometimes our experimental observations reveal conductivity spots elongated into $[110]$ or $[\bar{1}\bar{1}0]$ directions that may be due to subsurface reflectors lengthened in one of these directions. The implementation of a more complicated cavity shape should be done in the framework of a more basic approach describing nucleation and segregation of defects and inclusions in solids.

CONCLUSIONS

We have shown that the nanoinclusions buried close to a surface can be detected by STM due to the modifications in surface conductance caused by the near-surface localized QW. The spatial distribution of the perturbed conductance is largely determined by the shape of the (001) upper facet of

the buried nanocavity as well as by the anisotropy of the band structure of the crystal, in our case Cu. However, the detectable variation of the conductance far away from the cavity in particular directions shows the role of other types of facets, such as (110) and (111).

We developed a simple electron-interference model that is able to describe all the experimental details reasonably well, including the possibility to extract a rough estimation of the relevant parameters that govern the shape and location of the nanocavity. The rich details in our observations and the simplicity of our calculations could open up opportunities for a more detailed and systematic analysis of buried nano-objects. Specific objects and metal combinations could be used to tailor electron propagation and interferences over even longer distances with tunable symmetry. In case of magnetic nanoinclusions, one could even envision the observation of spin-resolved interference effects when combined with proper matrix material and dedicated tips coated with (anti)ferromagnetic material.

ACKNOWLEDGMENTS

This work was supported by the Dutch Technology foundation (STW) via the NWO VICI-grant "spintronics," as well as by the Dutch foundation for the Fundamental Research on Matter (FOM). We are grateful to K.-H. Rieder for valuable discussions.

-
- ¹X. Leyronas and M. Combescot, *Solid State Commun.* **119**, 631 (2001).
²G. Hormandinger and J. B. Pendry, *Surf. Sci.* **295**, 34 (1993).
³I. B. Altfeder, K. A. Matveev, and D. M. Chen, *Phys. Rev. Lett.* **78**, 2815 (1997).
⁴I. B. Altfeder, D. M. Chen, and K. A. Matveev, *Phys. Rev. Lett.* **80**, 4895 (1998).
⁵A. Mikkelsen and E. Lundgren, *Prog. Surf. Sci.* **80**, 1 (2005).
⁶K. Kobayashi, *Phys. Rev. B* **54**, 17029 (1996).
⁷A. Weismann, M. Wenderoth, N. Quaas, and R. G. Ulbrich, in *Abstracts of the 13th International Conference on Scanning Tunneling Microscopy/Spectroscopy and Related Technique*, Sapporo, 3–8 July 2005 (STM'05 Organizing Committee ISEBU Co. Ltd., Japan, 2005), p. 481.
⁸M. Schmid, W. Hebenstreit, P. Varga, and S. Crampin, *Phys. Rev. Lett.* **76**, 2298 (1996).
⁹M. Schmid, S. Crampin, and P. Varga, *J. Electron Spectrosc. Relat. Phenom.* **109**, 71 (2000).
¹⁰G. A. Burdick, *Phys. Rev.* **129**, 138 (1963).
¹¹J. Heil, M. Primke, A. Bohm, P. Wyder, B. Wolf, J. Major, and P. Keppeler, *Phys. Rev. B* **54**, R2280 (1996).
¹²F. J. Garcia-Vidal, P. L. deAndres, and F. Flores, *Phys. Rev. Lett.* **76**, 807 (1996).
¹³R. Grassme and P. Bussemer, *Phys. Lett. A* **175**, 441 (1993).
¹⁴M. F. Crommie, *J. Electron Spectrosc. Relat. Phenom.* **109**, 1 (2000).
¹⁵E. H. Sondheimer, *Adv. Phys.* **50**, 499 (2001); C. Kittel, *Introduction to Solid State Physics* (Wiley, New York, 1976).
¹⁶M. Prietsch, *Phys. Rep.* **253**, 163 (1995).
¹⁷M. Dähne-Prietsch and T. Kalka, *J. Electron Spectrosc. Relat. Phenom.* **109**, 211 (2000).
¹⁸C. Herring, *Phys. Rev.* **82**, 87 (1951).